Nucleation mechanism for hcpbcc phase transformation in shock compressed Zr

Nucleation mechanism for hcp→bcc phase transformation in shock compressed Zr

Hongxiang Zong[1, 2*], Ping He[1], Xiangdong Ding[1], Graeme J. Ackland[2]

[1]*State Key Laboratory for Mechanical Behavior of Materials, Xi'an Jiaotong University, Xi'an, Shanxi 710049, China*

[2]*Centre for Science at Extreme Conditions (CSEC), School of Physics and Astronomy, University of Edinburgh, Edinburgh EH9 3FD, UK*

Abstract

We present large-scale atomic simulations of shock induced phase transition in Zr assisted by machine learning method. The results indicate that there exists a critical piston velocity of $U_p \sim 0.85$ km/s, above which the product phase has changed from ω to bcc. Unlike the case in Fe, the shock induced hcp→bcc nucleation mechanism in hcp-Zr single-crystal shows significant dependence of crystal orientation. For shock along $[10\bar{1}0]$ direction, the hcp phase directly transforms into bcc as expected. However, for shock compression along [0001] and $[1\bar{2}10]$ directions, the hcp→bcc transformation occurs in quite a different manner, i.e., Zr single crystal transforms into a disordered intermediate that subsequently exhibits ultrafast crystallization of bcc phase within the timescales of sub-nanosecond. We associate such presence of disordered intermediate structure with the sluggishness of shear stress relaxation, which leads to an elastic unstable condition of the crystal during the first few picoseconds of uniaxial compression, and suggests that the fewer possible shear planes (related to Burgers mechanism) for [0001] and $[1\bar{2}10]$ shock loading is an underlying factor for the orientation dependence.

□. INTRODUCTION

Understanding the structural phase transition behaviors of solids under extreme compression is essential for materials science and a variety of applications [1–3]. One of the most studied cases is the pressure induced transformation from body-centered-cubic (bcc) into hexagonal-close-packed (hcp) structure. Since its discovery in iron at 13.0 GPa by Bancroft et al. in 1956, a wealth of knowledge has been gained on this transition through numerous studies [4–6]. Beside iron, the transitions between bcc and hcp have also been observed in many other metals during static or dynamic compression, such as Mg [7], Ba [8] and Zr [9]. It has been argued that the bcc→hcp transition is martensitic based upon its highly hysteretic nature [10], the influence of soft phonons [11] and the possible hcp variant selection [12]. The generally accepted mechanism is the so-called Burgers distortion that first established the crystallographic relationship between the bcc and hcp structures [13].

Previous studies on Fe have indicated that the bcc→hcp phase transition behavior is shear-stress dependent. This can be demonstrated by the scattered experimental data of the measured transformation pressure [14] and the multimillion-atom molecular dynamics (MD) simulations of shock compressed single crystals, which show orientation dependence [15]. For the high-pressure microstructure, some researchers have shown that when the shock compression is along the [001] crystal direction, the plane spacing between the (011) planes is not changed, and the *c/a* value of hcp iron is greater than 1.7, whereas the *c/a* value is close to the ideal value of 1.633 for shock compression along the [110] or [111]

direction [6]. Also, different from the case of [001] shock loading, the mixing of hcp and face-centered-cubic (fcc) structures is observed in [110] or [111] shock compressed Fe samples [16]. Despite all this, the underlying Burgers mechanism governing the bcc-hcp transformation was believed unchanged.

What's more, the shear stress experienced by materials under the static and dynamic compression can be radically different. In static measurements, the crystals are compressed under hydrostatic conditions, but under shock-wave loading, the sample is initially subjected to uniaxial strain. Hydrostatic conditions are approached only if significant plastic flow occurs or if significant shear stress is relieved during a phase transformation. Thus, if a transformation occurs before significant plastic flow, it may be along a very different pathway from a hydrostatically compressed sample. These differences may lead to a different orientation relation or even a different product phase [17]. In particular, at high piston velocity, there is less time for plastic deformation [18], and differences between dynamic and static compression should be intensified.

The group IV, hcp metal Zr, with transition temperatures and pressures that are relatively accessible, has served as an excellent test-bed for studying bcc-hcp phase transformation behavior under strongly driven conditions [19]. Zr exhibits the crystal structure sequence hcp→ω→bcc under quasi-static pressurization, with first-principles calculations indicating an increasing occupation of the d-states with pressure [20]. What's more, the amorphization of element Zr has been reported at high static pressure and low temperatures [21]. For the shock-induced phase

transformation in Zr, progress over the last three decades from recovery experiments and MD simulations [22–25] has largely focused on the hcp→ω phase transformations at low to medium shock pressures (below ~20 GPa) [23, 26, 27]. Less is known about how the hcp-Zr transforms into the bcc phase under strong shock pressure or higher piston velocity, and whether uniaxial compression changes the bcc-hcp transformation mechanism. Our recent simulation and experimental work [23] has shown, even under modest shock compression, that the phase transition pathway for hcp→ω in Zr has changed from the Silcock [28] to the Usikov-Zilbershtein pathway [29] at pressures above 27GPa.

In the present work, we have performed large-scale MD simulations of mono- and polycrystalline Zr governed by a machine learned interatomic potential, and investigated the kinetic effects on the hcp→bcc phase transformations under strong shock compression. Our results indicate that the transformation mechanism in Zr single crystals depends on the loading directions. Specifically, an amorphization intermediated indirect mechanism operates for [0001] or [$1\bar{2}10$] shocks. This is in contrast to the bcc→hcp phase transitions in shocked iron [18], which exhibit purely martensitic or displacive character.

□. METHODOLOGY

The motivation of this work is to understand the hcp-bcc phase transition behaviors in Zr under strong shock compression. Here, a combination of a machine-learning potential and large-scale MD simulation is used to simulate the shock induced hcp-bcc martensitic transformation in Zr. We developed a Gaussian

process based machine-learning interatomic potential to describe the phase transformation behaviors. The potential is directly learned from big database of first principles calculations that are related to the properties of different phases, enabling us to produce good results for the elastic properties, hcp, ω and bcc phase transformation behaviors, and defect formation energies [30].

The initial samples were prepared by constructing prefect hcp-Zr single crystals with the z axis parallel to the [0001], $[10\bar{1}0]$ or $[1\bar{2}10]$ crystallographic directions or hcp-Zr polycrystalline with grain size of about 7 nm. Typical samples have the dimensions of L_x = 75-100 Å, L_y = 75-100 Å and L_z = 1150–1250 Å. Periodic boundary conditions are applied in the x and y directions to mimic the uniaxial strain condition of planar shock loading. Prior to compression, the as-constructed samples are first equilibrated to achieve a minimum energy state using the conjugate gradient method, and then annealed at 300 K to their equilibrium, defect-free, hcp state. Shock waves are then generated along the z axis by taking one of the surface layers at the end of the sample as a reflecting "momentum mirror" or stationary piston and driving the sample towards the mirror at selected drift velocities. The drift velocity refers to the particle velocity behind the shock wave. The trajectory of each atom is then integrated by a predictor-corrector scheme with a time step of 1 fs. The molecular dynamics (MD) simulations were carried out using the LAMMPS codes [31]. The local structures are identified by a robust order parameter, which is based on the bond angle analysis and can average out considerable statistical fluctuations [32]. The visualization of atomic trajectories is done by the Open Visualization Tool (Ovito)

software [33].

□. RESULTS

A. EOS and principal Hugoniot

Before performing the NEMD simulations, we first determined the critical condition for the hcp-bcc phase transformation in Zr. Figure 1(a) shows the calculated enthalpy per atom of the hcp, ω and bcc phases upon static compression. Structural evolution and EOS of Zr are in agreement with previous studies i.e. we observe both the hcp→ω and ω→bcc phase transitions at critical pressures of 3.5 GPa and 12 GPa, which are in agreement with previous observations [19]. The similarity between the current simulations and the experiments allows meaningful study of pressure induced phase transition for Zr.

The principal Hugoniot of Zr in Fig. 1(b) shows a plot of shock pressure (P) versus particle velocity (U_p) with the data of McQueen et al. [34] and Greeff et al. [35]. Here, each dotted line marks the location of the solid-solid boundary. The two points of intersection in the Hugoniot curve of Fig. 1(b) reveal that the critical shock pressure of the hcp→ω and ω→bcc phase transition is around 7.54 GPa and 24.04 GPa, respectively. The shock pressure corresponding to the onset of the two transitions is well above the equilibrium transition pressure (Fig. 1(a)). Previous studies have suggested that the difference is due to a rate dependence of the hcp→ω and ω→bcc phase transformations in Zr [19]. Based on this, we select three different shock velocities around 0.85km/s.

B. Shock induced phase transition

Many studies have indicated that shock-induced phase transition and shock wave propagation in polycrystalline materials at the grain level are fundamentally different from those behaviors in single-crystals [36]. Therefore, both single crystal and polycrystal Zr samples are MD simulated and compared in the present work. For single crystal cases, three different shock loading directions $[10\bar{1}0]_\alpha$, $[1\bar{2}10]_\alpha$ and $[0001]_\alpha$ were selected to understand the orientation dependence of hcp-bcc transition behaviors. While for polycrystal Zr, we will focus on the grain boundaries activities and intra-granular processes.

1. Single crystal

Fig. 2 shows typical microstructure of $[10\bar{1}0]$ shock compressed Zr single crystals due to the change of piston velocity. Here, the shock wave is loaded from the left to the right, and the Zr atoms are colored according to their local atomic packing determined from characteristic bond angle analysis [32]. Consistent with the principal Hugoniot data, the formed phase has changed from ω to bcc as we increase the shock velocity from 0.54 km/s to 0.9 km/s. When shocked at low velocity of 0.54 km/s (or shock pressure of 16.84 GPa), Zr sample shows microstructure of lamellar-like ω nano-precipitates embedded in the hcp-Zr matrix, as shown in Fig. 2(b). The hcp→ω phase transition goes via a metastable bcc phase (blue atom regions in Fig. 2(a)), following the Usikov-Zilbershtein pathway [29]. We attribute such lamellar-like feature to the large in-plane strain constrain during the shock compression, which we will discuss latter. Our previous work has shown that the ω precipitates can further grow into the whole Zr samples after a relatively long time as the shock wave

propagates [24].

As expected, further enhancement of shock strength leads to the formation of stable bcc phase. Fig. 2(c) and 2(d) show the corresponding atomic configurations associated with an impactor velocity of 0.9 km/s (or shock pressure of 27.26 GPa), which consist of well-developed bcc phase and a few remnant ω nano-precipitates at the shock-wave front. A closer examination of the microstructure evolution indicates that most bcc grains are directly transformed from the hcp-Zr matrix, only a small fraction bcc phase being formed indirectly and proceeded by the formation of a metastable ω. All hcp-Zr lattices directly transform into well-developed bcc phase when we increase the loading pressure up to 30.87 GPa, as shown in Fig. 2(e) and 2(f). The absence of hcp→ω phase transition here indicates an overdriven condition in which the second wave of the hcp→bcc transition has overtaken the hcp→ω process.

It is important that we observed two different states of bcc phases: one (state A) is present as a metastable intermediated state during the hcp→ω transition at low shock velocity, while the other (state B) forms as the product phase in strong shock compressed Zr. To clarify their relationship, we compared the corresponding radius distribution functions (RDFs) of shock deformed regions (red boxes in Fig. 3(a)). As shown in Fig. 3(b), the two types of bcc structures have different lattice parameters. Therefore, we speculate that the occurrence of hcp→bcc (stable) phase transition under strong shock compression can be achieved by an isostructural bcc (metastable) → bcc (stable) phase transition, companied by the suppression of ω phase.

Subsequently, we studied the shock-velocity dependence of microstructure

evolution when shock compression along $[0001]_\alpha$ direction. At U_p = 0.54km/s, the main microstructural development within shocked Zr samples is dominated by the formation of ω phase. We find that the α→ω phase transformation in all the three cases proceeds via the formation of a metastable bcc phase (blue atom regions) at the shock wave front, with the ω phase (blue and orange chessboard regions) growing from bcc phase (Fig. 4(a) and 4(b)), consistent with our previous experimental observation [37]. At a critical shock velocity of 0.9 km/s, the main product phase gradually changes from ω to bcc phase, similar to the $[10\bar{1}0]_\alpha$ case, see Fig. 4(c) and 4(d). However, we find that the hcp→bcc phase transformation is mediated by the formation of a disordered region, instead of a direct transition pathway. To be specific, the hcp lattices first collapse into an amorphous state under strong shock compression loading, and then new bcc lattices are nucleated from the disordered regions. This indirect transition pathway leads to the formation of composite microstructures with bcc nano-precipitates embedded in the amorphous matrix, as shown in Fig. 4(c) and 4(e). These bcc embryos further grow at the expense of amorphous regions as the time goes (Fig. 4(d) and 4(f)). By looking at the neighborhood of the atoms before and after the transformation, we can see that the neighborhood is almost conserved after the formation of bcc phase. This means that the atoms do not have to move large distances in order to achieve the transformation, hence the observed transformation is prompt. The radial distribution function of atoms at the shock front (Fig. 5(a)), shows the presence of amorphous intermediate state. Experimental observations are beginning to support our findings, for example, amorphous-like structures have been

observed in previous quasi-static DAC experimental measurements of pure Zr [21, 38].

What's more, we find that the $[1\bar{2}10]_{\alpha}$ shocked Zr single crystal experiences a more complex phase transformation behavior than the other two cases. As shown in Fig. 6, we observe first, as the shock front passes the transformation region, the occurrence of hcp→ω phase transition for all shock velocities from 0.7 km/s to 1.0 km/s. This is quite different from the $[10\bar{1}0]$ and [0001] shock directions, which show no ω phase above the critical shock velocity of ~0.85 km/s. Fig. 6(a) and 6(b) show the typical microstructure evolution of shock compressed Zr at low shock velocity of 0.70 km/s (or shock pressure of 21.68GPa), which only includes the formation of ω phase. Under stronger shock compression loading, we show that following the process of ω phase formation, ω-Zr converts subsequently to bcc phase by means of an indirect transition pathway, i.e., ω-Zr lattices first change into an intermediate state, followed by the nucleation and growth of new bcc phase (Fig. 6(c) -6(f)). The structures of the intermediate state and the subsequent new phases in the same region are identified via the RDFs, as shown in Fig. 5(b). The very weak peaks in the RDF at 8 ps indicate that the intermediate phase possesses an amorphous-like structure. After 18 ps shock loading, RDF has main peaks characteristic of bcc. This further confirms the nucleation and growth of bcc phase within the intermediate amorphous regions.

We further explored the orientation relationships between the hcp and bcc phases during the phase transition. Unlike the post-mortem microstructures analysis in shock

experiments, the MD simulations enable us to evaluate the crystallographic orientations of coexisting phases directly. In Fig. 7, we have selected atomic configurations containing both parent phase and product phases from 0.9 km/s shock loaded Zr samples. Fig. 7(a), 7(b) and 7(c) show the slices collected from the $[10\bar{1}0]_\alpha$, $[1\bar{2}10]_\alpha$ and $[0001]_\alpha$ shock compressed Zr single crystals, respectively. Indexing of the parallel atomic stacking planes of the two phases in all the three cases has shown that the arrangement of the two lattices for hcp and bcc leads to the same OR, $(0001)_{\text{hcp}} \parallel (1\bar{1}0)_{\text{bcc}}$. This indicates that the ORs between the primary hcp lattices and new formed bcc phases in Zr are the same as the ORs of the Burgers mechanism [13], although their phase transformation pathway may change.

To determine the nucleation rate of bcc phase along the indirect transformation path, we apply the constant-stress Hugoniostat technique [39] to simulation the homogenous crystallization process in Zr under strong shock compression. Here, we take the [0001] shocked single crystal as an example, at 30 GPa, equivalent to the shock-wave loading with the impactor velocity of 1.0 km/s. Snapshots in Fig. 8 illustrate a typical nucleation and growth process of the bcc-Zr phase. Figure 8(a) shows the appearance of bcc nuclei several lattice spacings in diameter. With time evolution, some of these nuclei disappear and some grow steadily into grains of a larger size, and these grains are well separated from each other (see SI movie1). Figure 8(b) and 8(c) shows the rapid growth stage of bcc grains, which is accompanied by the coalescence of these grains at the grain boundaries. Note that it takes up to 300 ps to form the well-defined “coarse grains” of bcc phase, as shown in

Fig. 8(d). This indicates that the recrystallization of bcc-Zr phase is slow relative to atomic vibrations, so the intermediate amorphous phase is thermodynamically well-defined. However, sub-nanosecond recrystallization is fast on experimental timescales, which explains why the intermediate amorphous phase cannot be observed with post-mortem microstructures analysis, and further *in-situ* investigation should be carried out to elucidate this indirect transformation pathway.

2. Polycrystalline

It is likely that the phase transition behaviors of shocked polycrystalline Zr are quite different from that in single crystals due to plasticity linked to grain boundaries (GB) and intragranular processes [40, 41]. Therefore, we analyzed the response of polycrystalline α-Zr to a strong shockwave loading. Fig. 9 shows the different deformation stages for a α-Zr polycrystal under shock compression with a piston velocity of 1.0 km/s. As shown in Fig. 9, our initial structure of the Zr polycrystal had nano-sized crystal grains with clean grain boundaries (white lines in Fig. 9(a)) and a porosity of 0.26%. These relative-open grain boundary regions are among the most vulnerable places in Zr polycrystal, and could be conducive to the strain accommodation under shock compression. As shown in Fig. 9, we immediately observe uniaxial elastic deformation, followed by some GB activities. In Fig. 9(a) and 9(b), we show a typical grain boundary migration process [42] indicated by the red lines. Further loading leads to the occurrence of the hcp→bcc structural phase transformation in the region behind the shock front (Fig. 9(c)). The propagation of the shock wave then leads to the rapid transformation of each grain to bcc phase (Fig.

9(d)). We note that there was no distinct amorphous intermediate structure within the grains during the phase transformation process, which is quite different from the response of Zr single crystals.

□. Discussions

The hcp→bcc phase transformation paths in shocked Zr single crystals show strong orientation dependence. In particular, the hcp→bcc phase transformations in [0001] and [$1\bar{2}10$] strong-shock-compressed hcp-Zr single crystals follows an indirect transformation path, and not the usual Burgers mechanism. Our discussions below indicate that this is related to the incompatibility of the Burgers mechanism and uniaxial compression combined with the difficulty of local shear stress relaxation. In the following, we will focus on the aspect of local shear stress relaxation and its crystallographic correlation with the phase transformation mechanisms.

A. Shear stress relaxation

The shock compression generates, by nature of the uniaxial strain state imposed, simultaneous and coupled hydrostatic and shear stresses. Polycrystal Zr has both grain boundaries and heterogeneity among grains, which facilitate rapid plastic relaxation upon shock compression. Fig. 10 shows the ratio of the shear stress to the hydrostatic transformation pressure (λ) [43] plotted as a function of peak pressure for both shock-loaded polycrystal and [0001] single crystal. The single crystal compressed along [0001] supports 60% higher shear stress than the Zr polycrystals (Fig. 10), indicating the important role of grain boundary plasticity in the local shear stress relaxation.

The mechanism for the fast disordering of hcp-Zr may be associated with an elastic instability which can be evaluated by the Born elastic stability criteria [44]. For the hcp lattice, the following three Born stability criteria must be met [45]: (1) $B_1 = C_{11} - |C_{12}| > 0$, (2) $B_2 = (C_{11} + C_{12})C_{13} - 2C_{13}^2 > 0$ and (3) $B_3 = (C_{11}\text{-}C_{12})C_{44} - 2C_{14}^2 > 0$, where C_{ij} is the corresponding elastic constants. For [0001] or [1-210] shocked Zr single crystal, the amorphization during the first few picoseconds of shock compression may be caused, at least in part, by an elastic instability. To investigate the role of such effect, we compared the Born stability criteria of hcp-Zr under hydrostatic pressure and uniaxial strain. A difference between hydrostatic and shock loading is that the shock applies uniaxial strain. In Fig. 11, three Born stability criteria are plotted as a function of pressure by using first-principle calculation. In the hydrostatic case, the Zr single crystals remain stable up to 30 GPa (Fig. 11). In contrast, our result of the uniaxial case shows that B_1 and B_2 become negative beyond ~20 GPa (Fig. 11). This break-down of the Born elastic stability criteria implies the hcp crystal will be subject to spontaneous disordering on the timescale of elastic vibrations.

The strong shock-wave loading provides the driving energy that nucleates the amorphous phase. This was previously analyzed for Si, Ge, and B_4C with the Patel-Cohen methodology [46]. The same formalism can be applied here, based on the effects of pressure and shear stresses on the thermodynamics of phase equilibria, and it has the following form:

$$W = P\varepsilon_T + \tau\gamma \quad (1)$$

where P is the pressure (hydrostatic component of stress), ε_T is the amorphization normal strain, τ is the shear stress (here we assume maximum shear 45° away from the loading direction), and γ is the amorphization shear strain. As shown in Fig. 10, the increase in W with shock stress is monotonic and reaches a value of up to 4.0 GJ/m^3 at 30 GPa, a typical pressure for the presence of amorphous metastable phase. This can provide the driving energy that overcomes the activation barrier and nucleates the amorphous regions in shock compressed Zr single crystals.

B. Transformation strain and crystal symmetry

In Fig. 12, we consider a pure hcp-Zr single crystal sample. In the generally-accepted Burgers mechanism, the hcp→bcc transition involves simultaneous shear deformation of (0001) planes with alternating shuffle of the adjacent planes. In this scenario, the (0001) planes of the parent hcp crystal undergo shearing via the coupling of a compressional strain along $[10\bar{1}0]$ and a tensile strain along $[1\bar{2}10]$, wherein the reshaped (0001) hcp planes become the $(1\bar{1}0)$ planes of the new bcc crystal. This means that as a result of hcp→bcc phase transition the crystal will contract along the $[10\bar{1}0]$ direction and elongate in the $[1\bar{2}10]$ direction. Under $[10\bar{1}0]$-hcp shock wave loading, the lattice compression parallel to the loading direction will facilitate the compressive strain, thus favoring the formation of bcc phase (Fig. 12(a)). On the other hand, shock along $[1\bar{2}10]$ directions, provides a lattice compression in the direction where the Burgers mechanism requires elongation, thus deterring the direct ω→bcc phase transformation under shock loading (Fig. 12(b2)).

The situation is similar when Zr single crystal undergoes [0001] shock compression, as shown in Fig. 12(c). Without significant shear strain relaxation under strong shock wave loading, the uniaxial compressive strain perpendicular to the (0001) plane cannot provide shearing that required to initiate the $(0001)_{hcp} \rightarrow (1\bar{1}0)_{bcc}$ transformation [47]. Even at low shock velocity and with moderate local shear stress relaxation, the hcp→bcc phase transformation occurs in a twinning manner in order to accommodate the accompanying large $(0001)_{hcp}$ in-plane transformation strain (around 8%) [48]. The large in-plane strain mismatch between hcp and bcc phase should be a high energy barrier for the phase transition during the [0001] shock compression. What's more, the reduction of inter-layer distance may hinder the shuffle of the adjacent atomic planes. No such orientational issues apply to forming an amorphous phase: although the transformation to bcc is thermodynamically preferred, if the kinetic transformation pathway to bcc is hindered, amorphization occurs first.

If there is no rapid mechanism for plasticity, and the direct hcp→bcc phase transformation is hindered, a large uniaxial elastic strain is inevitable. We have shown that this large uniaxial strain results in elastic instabilities in the hcp lattices, and amorphization can release deviatoric stress. Thus the stress in the amorphous region is close to hydrostatic. This enables the formation by nucleation and growth of the bcc phase. To confirm this quantitatively, we have calculated the corresponding potential energy difference among the amorphous, hcp and bcc phases, as shown in Fig. 13. Compared with uniaxial deformed hcp-Zr, the hydrostatic, amorphous structure becomes preferred energetically as we increase the uniaxial strain, similar to that

occurs in magnesium under high strain rate compression [49]. The elastic instability means the hcp-amorphous occurs spontaneously. The bcc lattice always has the lowest energy under the comparable hydrostatic pressure, which ultimately drives the formation of bcc phase from within amorphous regions.

Using the concept of amorphous intermediates, we can also explain the occurrence of hcp→ω phase transformation under high shock velocity loading along $[1\bar{2}10]$ directions. Our previous works have shown that the ORs of the hcp→ω phase transformation in Zr are consistent with the experimentally observed Silcock pathway [28]. The Silcock mechanism combines a compression strain (e_{xx} = -0.05) along $[1\bar{2}10]$ direction with a tensile strain (e_{zz} = 0.05) along [0001] direction, which produces a final ω cell from our hcp-Zr cell. Accordingly, the uniaxial compression strain parallel to the loading direction caters to the formation of metastable ω lattices in Zr single crystals when a shock compression is applied along the $[1\bar{2}10]$ direction (Fig. 12(b1)).

We note that the forward and reverse bcc-hcp transformation should be asymmetric for single crystals due to the different ability of transformation shearing under shock compression. Considering the Burgers mechanism for example, for the forward bcc→hcp phase transformation, $\{110\}_{bcc}\rightarrow(0001)_{hcp}$, there are six orientations of $\{110\}_{bcc}$ planes in a bcc single crystal meaning at least two active shear planes in response to any uniaxial compression [50]. In contrast, for the reverse hcp→bcc phase transformation, there exists only one transformation shear plane i.e., $(0001)_{hcp}$, so for some directions of uniaxial compression there is no driving force for

the hcp→bcc phase transformation via the Burgers mechanism.

□. SUMMARY AND CONCLUSIONS

In summary, the current findings not only show the first atom-level picture of how the hcp→bcc structural transformation occurs in Zr single crystals and polycrystals under strong shock compression, but also we elucidate the dependence of the phase transition on shock direction. Above a critical piston velocity, Zr single-crystals experience a loading-orientation dependent hcp→bcc phase transformation. For $[10\bar{1}0]$ shock compression, MD simulation results give the direct transformation path, similar to the bcc→hcp transition in shocked Fe. What is new is that hcp-Zr single crystals undergo a rapid structural instability to an amorphous state and subsequent crystallization of bcc lattices when they are subjected to shock compression along the [0001] and $[1\bar{2}10]$ orientation, the uniaxial compression strain of which are unfavorable for the Burgers distortion. We propose a hypothesis that the unique (0001) plane in hcp crystals compared with the multiple (110) planes in bcc is responsible for the anisotropic phase transformation pathway. A similar argument applies to the hcp→ω phase transition and the Silcock mechanism.

Our predicted new hcp→bcc phase transformation mechanism involves an intermediate amorphous phase, or in the case of $[1\bar{2}10]_{\alpha}$ an intermediate ω phase, which persist on sub-nanosecond timescales. Similar to that in shocked fused silica and quartz [45], the nucleation and growth of new phase can last for the timescale of nanoseconds.

The key insight is that transformation to an amorphous phase is always rapid,

once the parent phase becomes unstable. Under dynamic compression, behind a strong shock, the parent phase becomes unstable to many possible product phases. The one which is observed initially is the one which can be reached fastest, and the relative speed of transition depends on the crystallographic details. The emergence of *in-situ* and high resolution temporal and spatial probes (e.g. coherent diffraction using XFEL's at facilities such as LCLS), provides an excellent near term opportunity to validate our predictions relating to the phase transformation behaviors under shock environments in high-purity single crystals of Zr.

ACKNOWLEDGEMENTS

This work was supported by Key Technologies R&D Program (2017YFB0702401), the National Natural Science Foundation of China (51320105014, 51871177 and 51931004), the ERC grant "Hecate" and the 111 project 2.0 (BP2018008).

References:

[1] Q. Xiong, T. Kitamura, and Z. Li, J. Appl. Phys. 125, 194302 (2019).

[2] S.J. Tracy, R.F. Smith, J.K. Wicks, D.E. Fratanduono, A.E. Gleason, C.A. Bolme, V.B. Prakapenka, S. Speziale, K. Appel, A. Fernandez-Pañella, H.J. Lee, A. MacKinnon, F. Tavella, J.H. Eggert, and T.S. Duffy, Phys. Rev. B. 99, 214106 (2019).

[3] H. Zong, X. Ding, T. Lookman, J. Li, J. Sun, E.K. Cerreta, J.P. Escobedo, F.L. Addessio, and C.A. Bronkhorst, Phys. Rev. B. 89, 220101(R) (2014).

[4] K.J. Caspersen, A. Lew, M. Ortiz, and E.A. Carter, Phys. Rev. Lett. 93, 115501 (2004).

[5] R. D. Taylor, M. P. Pasternak, and R. Jeanloz, J. Appl. Phys. 69, 6126 (1991).

[6] D.H. Kalantar, J.F. Belak, G.W. Collins, J.D. Colvin, H.M. Davies, J.H. Eggert, T.C. Germann, J. Hawreliak, B.L. Holian, K. Kadau, P.S. Lomdahl, H.E. Lorenzana, M.A. Meyers, K. Rosolankova, M.S. Schneider, J. Sheppard, J.S. Stölken, and J.S. Wark, Phys. Rev. Lett. 95, 075502 (2005).

[7] R.M. Wentzcovitch, Phys. Rev. B. 50, 10358 (1994).

[8] Y. Chen, K. M. Ho, and B. N. Harmon, Phys. Rev. B. 37, 283 (1988).

[9] M.T. Pérez-Prado and A.P. Zhilyaev, Phys. Rev. Lett. 102, 175504 (2009).

[10] F. M. Wang and R. Ingalls, Phys. Rev. B. 57, 5647 (1998).

[11] U. Pinsook and G.J. Ackland, Phys. Rev. B. 59, 13642 (1999).

[12] L. Gao, X. Ding, H. Zong, T. Lookman, J. Sun, X. Ren, and A. Saxena, Acta Mater. 66, 69-78 (2014).

[13] W.G. Burgers, Physica. 1, 561 (1934).

[14] B. Yaakobi, T.R. Boehly, D.D. Meyerhofer, T.J.B. Collins, B.A. Remington, P.G. Allen, S.M. Pollaine, H.E. Lorenzana, and J.H. Eggert, Phys. Rev. Lett. 95, 075501 (2005).

[15] K. Kadau, T.C. Germann, P.S. Lomdahl, and B.L. Holian, Phys. Rev. B. 72, 064120 (2005).

[16] J.A. Hawreliak, D.H. Kalantar, J.S. Stölken, B.A. Remington, H.E. Lorenzana, and J.S. Wark, Phys. Rev. B. 78, 220101(R) (2008).

[17] J. Hawreliak, J.D. Colvin, J.H. Eggert, D.H. Kalantar, H.E. Lorenzana, J. S. Stölken, H.M. Davies, T.C. Germann, B.L. Holian, K. Kadau, P.S. Lomdahl, A. Higginbotham, K. Rosolankova, J. Sheppard, and J.S. Wark, Phys. Rev. B. 74, 184107 (2006).

[18] K. Wang, S. Xiao, H. Deng, W. Zhu, and W. Hu, Int. J. Plast. 59, 180 (2014).

[19] C.W. Greeff, Model Simul Mater Sc. 13, 1015 (2005).

[20] R. Ahuja, J.M. Wills, B. Johansson, and O. Eriksson, Phys. Rev. B 48, 16269 (1993).

[21] J. Zhang, Y. Zhao, C. Pantea, J. Qian, L.L. Daemen, P.A. Rigg, R.S. Hixson, C.W. Greeff, G.T. Gray, Y. Yang, L. Wang, Y. Wang, and T. Uchida, J. Phys. Chem. Solids 66, 1213 (2005).

[22] H. Zong, T. Lookman, X. Ding, C. Nisoli, D. Brown, S.R. Niezgoda, and S. Jun, Acta Mater. 77, 191 (2014).

[23] H. Zong, Y. Luo, X. Ding, T. Lookman, and G.J. Ackland, Acta Mater. 162, 126 (2019).

[24] C. Nisoli, H. Zong, S.R. Niezgoda, D.W. Brown, and T. Lookman, Acta Mater. 108, 138 (2016).

[25] E.K. Cerreta, F.L. Addessio, C.A. Bronkhorst, D.W. Brown, J.P. Escobedo, S.J. Fensin, G.T. GrayIII, T. Lookman, P.A. Rigg, and C.P. Trujillo, J. Phys. Conf. Ser. 500, 032003 (2014).

[26] D.W. Brown, J.D. Almer, L. Balogh, E.K. Cerreta, B. Clausen, J.P. Escobedo-Diaz, T.A. Sisneros, P.L. Mosbrucker, E.F. Tulk, and S.C. Vogel, Acta Mater. 67, 383 (2014).

[27] G. Jyoti, R. Tewari, K.D. Joshi, D. Srivastava, G.K. Dey, S.C. Gupta, S.K. Sikka, and S. Banerjee, Defect Diffus. Forum 279, 133 (2008).

[28] J.M. Silcock, Acta Metall. 6, 481 (1958).

[29] M.P. Usikov, and V.A. Zilbershtein, Phys. Status Solidi 19, 53 (1973).

[30] H. Zong, G. Pilania, X. Ding, G.J. Ackland, and T. Lookman, Npj Comput. Mater. 4, 48 (2018).

[31] S. Plimpton, J. Comput. Phys. 117, 1 (1995).

[32] G.J. Ackland, and A.P. Jones, Phys. Rev. B. 73, 054104 (2006).

[33] A. Stukowski, Model. Simul. Mater. Sci. Eng. 18, 015012 (2010).

[34] R. Kinslow, High-Velocity Impact Phenomena (Academic, New York, 1970).

[35] C.W. Greeff, D.R. Trinkle, and R.C. Albers, J. Appl. Phys. 90, 2221 (2001).

[36] A. B. Sawaoka, Shock Waves in Materials Science (Springer, Tokyo, 1992).

[37] M. Armstrong, H. Radousky, R. Austin, E. Stavrou, H. Zong, G. Ackland, S. Brown, J. Crowhurst, A. Gleason, E. Granados, P. Grivickas, N. Holtgrewe, H. Lee, T. Li, S. Lobanov, J. McKeown, R. Nagler, I. Nam, A. Nelson, V. Prakapenka, C. Prescher, J. Roehling, N. Teslich, P. Walter, A. Goncharov, J. Belof, arXiv:1808.02181.

[38] Y. Wang, Y.Z. Fang, T. Kikegawa, C. Lathe, K. Saksl, H. Franz, J.R. Schneider, L. Gerward, F.M. Wu, J.F. Liu, and J.Z. Jiang, Phys. Rev. Lett. 95, 155501 (2005).

[39] R. Ravelo, B.L. Holian, T.C. Germann, and P.S. Lomdahl, Phys. Rev. B. 70, 014103 (2004).

[40] S. V. Razorenov, A.S. Savinykh, and E.B. Zaretsky, Tech. Phys. 58, 1437 (2013).

[41] G.J. Kleiser, L.C. Chhabildas, and W.D. Reinhart, Int. J. Impact Eng. 38, 473 (2011).

[42] K. Wang, W. Zhu, S. Xiao, K. Chen, H. Deng, and W. Hu, Int. J. Plast. 71, 218 (2015).

[43] S. Zhao, R. Flanagan, E.N. Hahn, B. Kad, B.A. Remington, C.E. Wehrenberg, R. Cauble, K. More, and M.A. Meyers, Acta Mater. 158, 206 (2018).

[44] F. Mouhat, and F.X. Coudert, Phys. Rev. B. 90, 224104 (2014).

[45] Y. Shen, S.B. Jester, T. Qi, and E.J. Reed, Nat. Mater. 15, 60 (2016).

[46] J.R. Patel, and M. Cohen, Acta Metall. 1, 531 (1953).

[47] H. Zong, T. Lookman, X. Ding, S.N. Luo, and J. Sun, Acta Mater. 65, 10 (2014).

[48] S.G. Song, and G.T. Gray, Philos. Mag. A. 71, 275 (1995).

[49] S. Wang, H. Pan, A. He, P. Wang, and F. Zhang, Phys. Rev. B. 100, 214106 (2019).

[50] H. Djohari, F. Milstein, and D. Maroudas, Phys. Rev. B. 79, 174109 (2009).

Figure captions

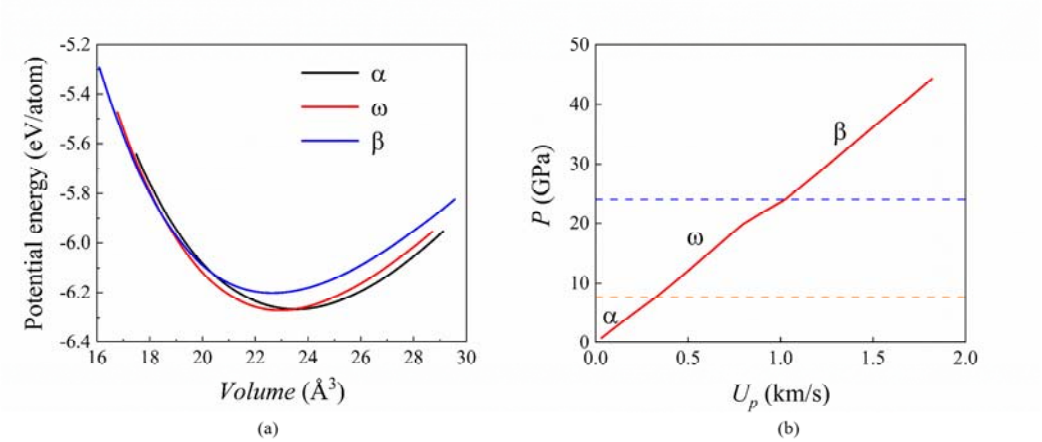

FIG. 1. The phase stability and shock Hugoniot of zirconium under compression. (a) Potential energy of different phases as a function of volume using the present machine learning potential. (b) The shock Hugoniot for Zr a plot of shock pressure (P) vs particle velocity (U_p), was determined from the multiphase model developed by Greeff [19]. Both data indicate a successively α (hcp) → ω(hex) → β (bcc) phase transition with increasing pressure.

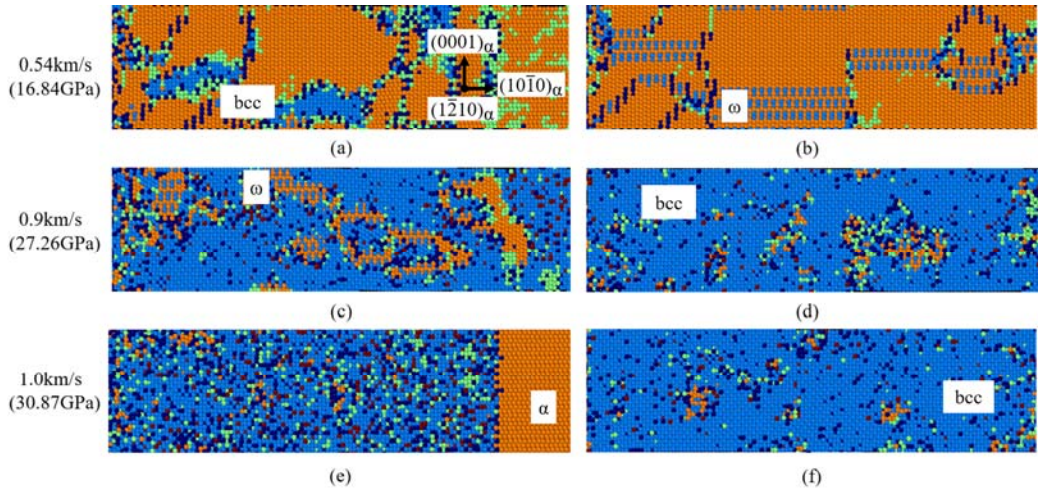

FIG. 2. Microstructural development of $[10\bar{1}0]_\alpha$ shocked Zr single crystals with piston velocities from 0.54 km/s to 1.0 km/s. The shock direction is from left to right. The left panel and the right panel show typical microstructure at 8 ps and 18 ps, respectively. Atoms with an hcp environment are shown as orange spheres and represent the α phase, pure blue regions show the location of bcc phase, whereas the blue and orange regions mark the ω phase, and other colors belong to defects. The increase of shock strength brings the shocked α-Zr single crystals to the final state from ω to bcc phase.

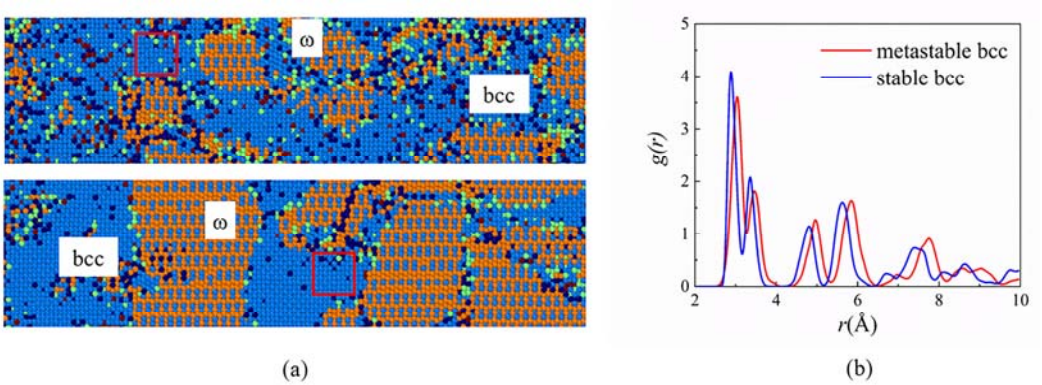

FIG. 3. Structural comparison of metastable bcc intermediate (state A) and finial bcc product phase (state B). (a) Typical microstructures of $[10\bar{1}0]_{\alpha}$ shocked Zr with the piston velocity of 0.8 km/s (or shock pressure of 25.28 GPa), showing the phase transition sequence of hcp → bcc (metastable) → ω → bcc (stable). The red boxes mark the regions that are used to calculate the radial distribution functions (RDFs). The color coding and labels are the same with Fig. 2. (b) The corresponding RDFs of two states of bcc structures. It shows that the two types of bcc phase differ in the lattice constants.

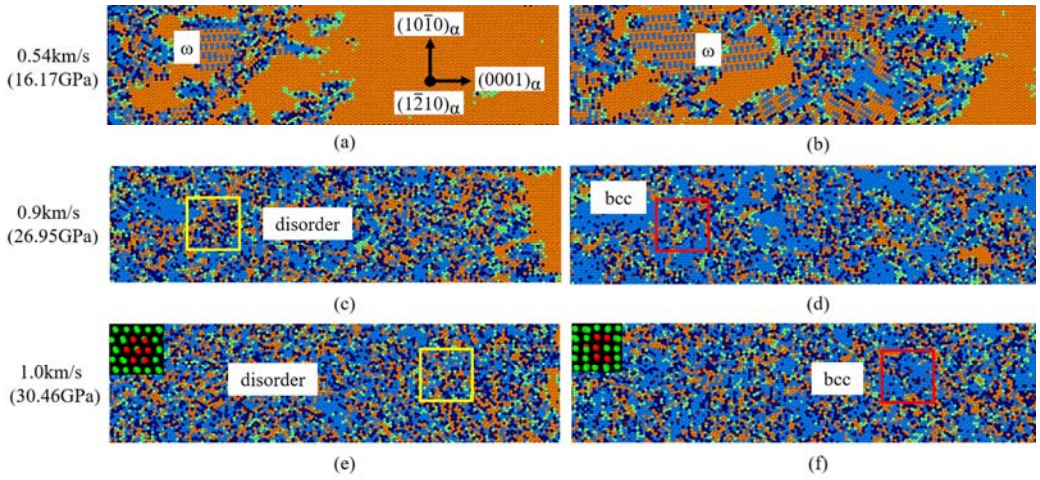

FIG. 4. Snapshots of the phase transformation processes in $[0001]_\alpha$ shocked Zr single crystals with different piston velocities. (a) and (b) The nucleation and growth of ω phase under 0.54 km/s shock compression, intermediated by the formation of metastable bcc. (c) and (d) The formation of bcc phase from the hcp-Zr matrix, accompanied by a few volume fraction of amorphous intermediate. (e) and (f) Under 1.0 km/s shock loading, the hcp-Zr lattices first collapse into obvious disordered region, where new bcc grains forms within the disordered region subsequently. The inset shows the neighborhood information of the atoms before and after the transformation. The color coding are the same with Fig. 2, and the boxes locate the regions for the calculation of local radial distribution functions.

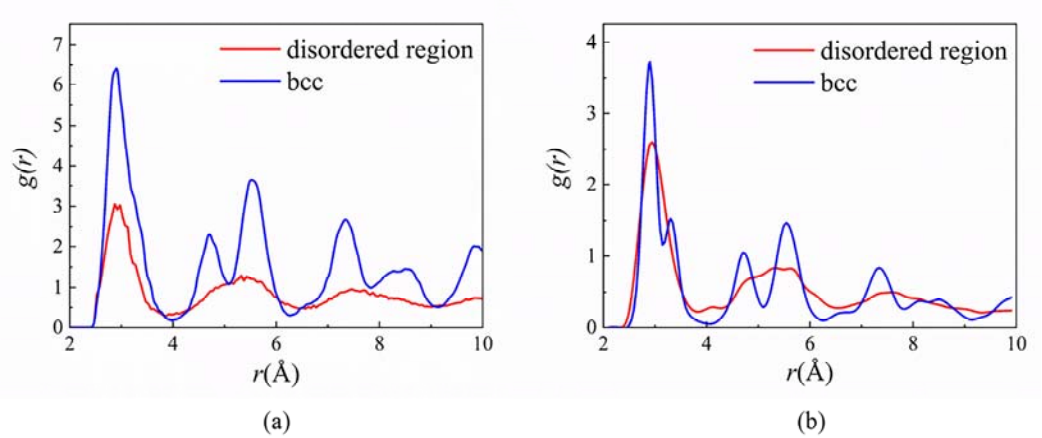

FIG. 5. Comparison of the radial distribution functions (RDFs) of disordered regions and crystallized bcc grains for (a) $[0001]_{\alpha}$ shocked Zr single crystals and (b) $[1\bar{2}10]_{\alpha}$ shocked Zr single crystals. It indicates that the disordered regions in both cases have a different structural feature from the bcc phase.

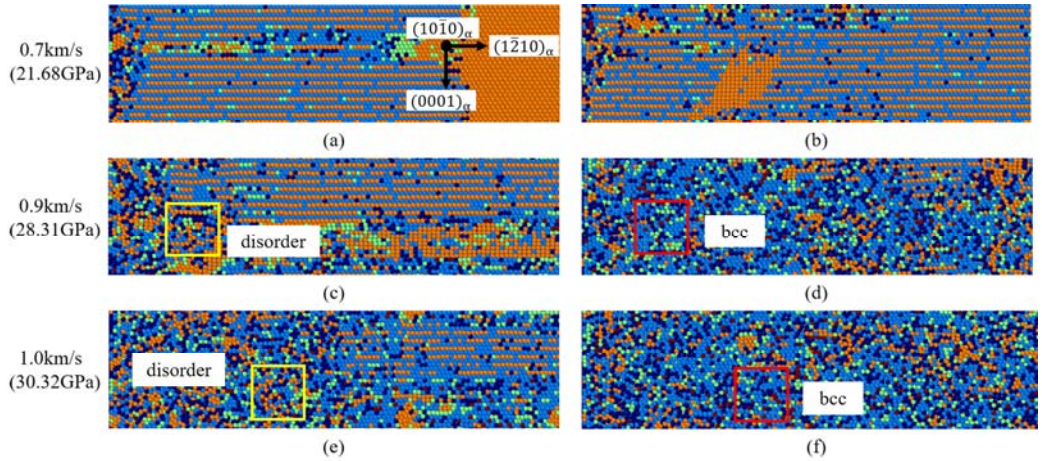

FIG. 6. Snapshots of the phase transformation processes in $[1\bar{2}10]_\alpha$ shocked Zr single crystals with different piston velocities. (a) and (b) The formation of ω phase in 0.7 km/s shocked Zr single crystal. (c) to (f) For shock velocity above 0.9 km/s, the α (hcp) →ω phase transformation is followed by the formation of disordered regions, and then new bcc grains forms at the expense of the disordered region. The color coding are the same with Fig. 2, and the boxes locate the regions for the calculation of local radial distribution functions.

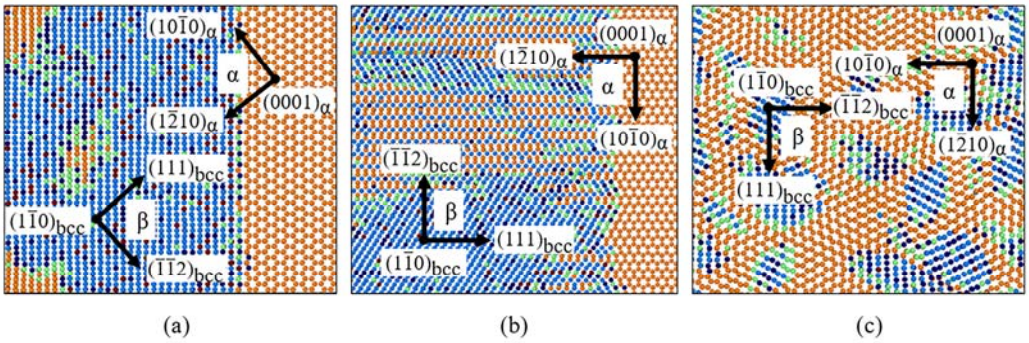

FIG. 7. Orientation relationships between hcp phase and bcc phase within the shocked samples. (a)-(c) represent typical slices of the bcc-hcp phase coexistence obtained from Fig. 2(e), Fig. 4(f) and Fig. 6(f), respectively. The orientation relationships between hcp phase and bcc phase in (a) $[10\bar{1}0]_\alpha$, (b) $[1\bar{2}10]_\alpha$ and (c) $[0001]_\alpha$ shocked Zr single crystals are all accord with the Burgers mechanism [13]. The color coding is the same with Fig. 2.

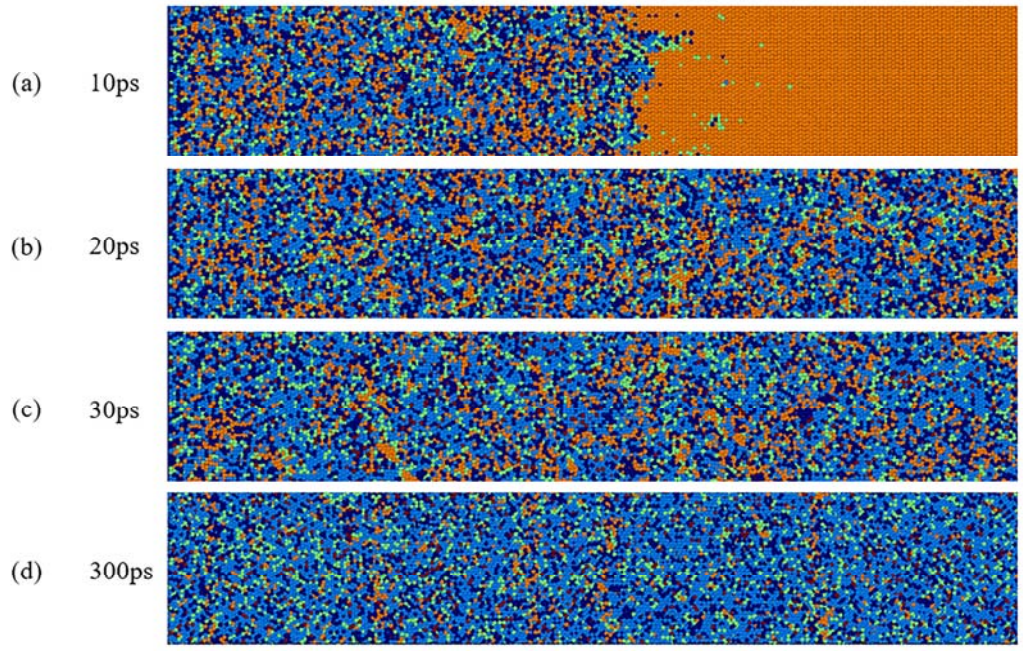

FIG. 8. Microstructural evolution of $[0001]_{\alpha}$ shocked Zr single crystal showing the crystallization of bcc phase from the metastable amorphous phase. (a) and (b) show the initial amorphization and bcc nucleation for the shock-wave swept regions. (c) and (d) present the following explosive grain growth and coalescence of bcc phase, leading to the formation of bcc-Zr polycrystal. The whole nucleation and growth process lasts about 300 ps. All viewing directions are parallel to the shock propagation. The color coding is the same with Fig. 2.

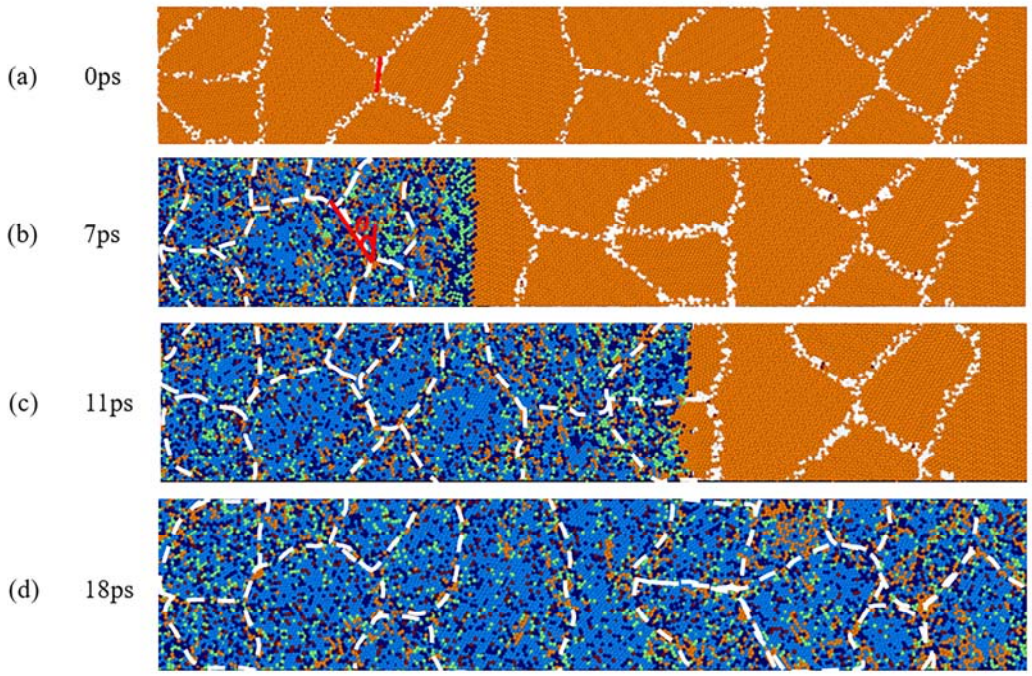

FIG. 9. Microstructure evolution of 1.0 km/s or 30.01GPa shocked Zr polycrystal showing the interaction between inter-grain activities and hcp→bcc phase transformation. (a)-(d) represent the atomic configurations after shocked 0 ps, 7 ps, 11 ps and 18 ps respectively. The red lines in (a) and (b) shows a typical grain boundary migration event under shock compression. The inter-grain and grain boundary activities help shear stress relaxation and the hcp→bcc transformation with direct pathway. The color coding is the same with Fig. 2, and the white dash curves mark the grain boundaries.

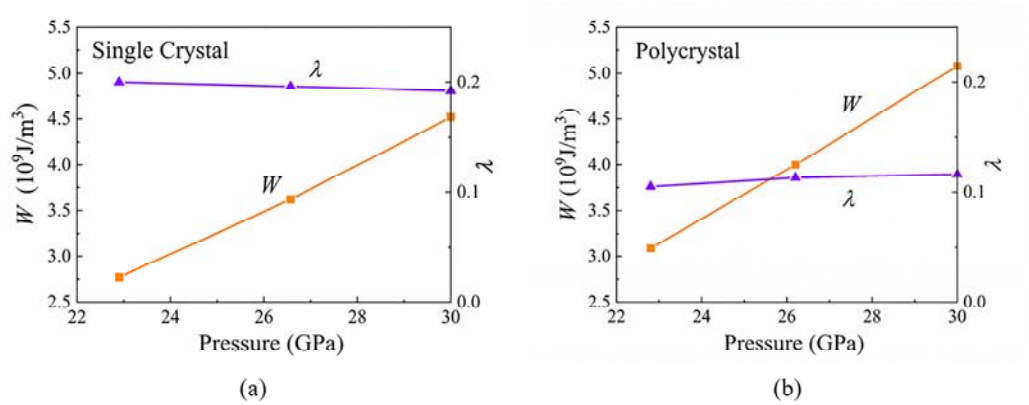

FIG. 10. Effect of longitudinal shock pressure on the shear level parameter (λ) and amorphization work (W) for (a) Zr single crystals and (b) Zr polycrystals. Here, the shear level parameter λ is defined as the ratio of the shear stress to the hydrostatic transformation pressure [43], and the amorphization work is evaluated from the Patel-Cohen model [46].

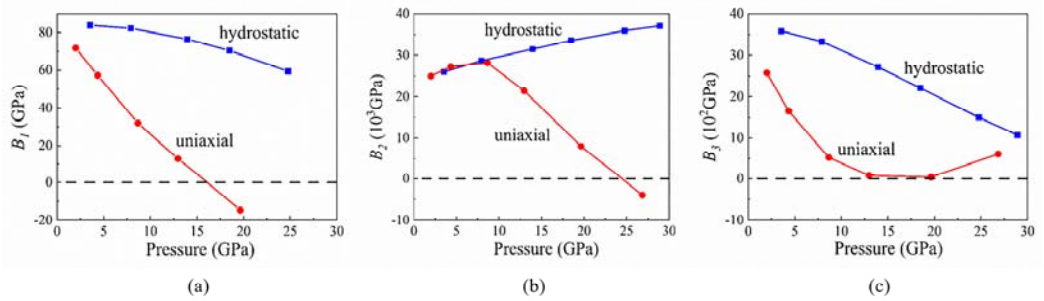

FIG. 11. A comparison of between *c*-axis uniaxial strain-induced and hydrostatic pressure-induced Zr amorphization. Three Born stability criteria criteria B_i (i =1, 2 and 3) are plotted with respect to either the hydrostatic pressure P_{hydro} (blue curve) or the stress along the uniaxial strain direction P_{uniaxial} (red curve). All the data are obtained from first-principle calculations. The Born criteria show that the uniaxial case is more inclined to become Born elastic unstable at high P_{uniaxial}.

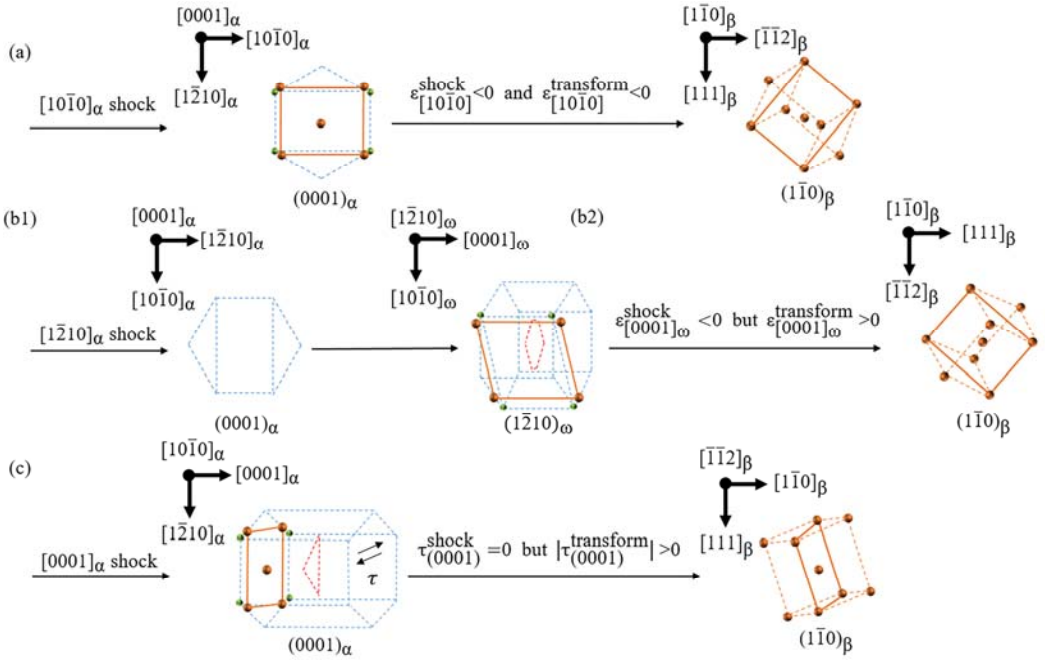

FIG. 12. Schematic illustration of the competition between lattice shape change of phase transformation and uniaxial compression strain of shock loading. (a) The hcp→bcc phase transition requires the hcp-Zr crystal to contract along the $[10\bar{1}0]$ direction, in line with the uniaxial compressive strain applied by shock loading. (b) The strong shock loading along $[1\bar{2}10]_\alpha$ direction leads to a successively hcp → ω → bcc phase transition. The $[1\bar{2}10]_\alpha$ compressive strain of shock is a barrier for the formation of bcc phase as the phase transition requires a tensile strain along this direction. (c) The *c*-axial compressive strain of shock can hardly provide any in-plane shear strain that is required for the hcp→bcc phase transition.

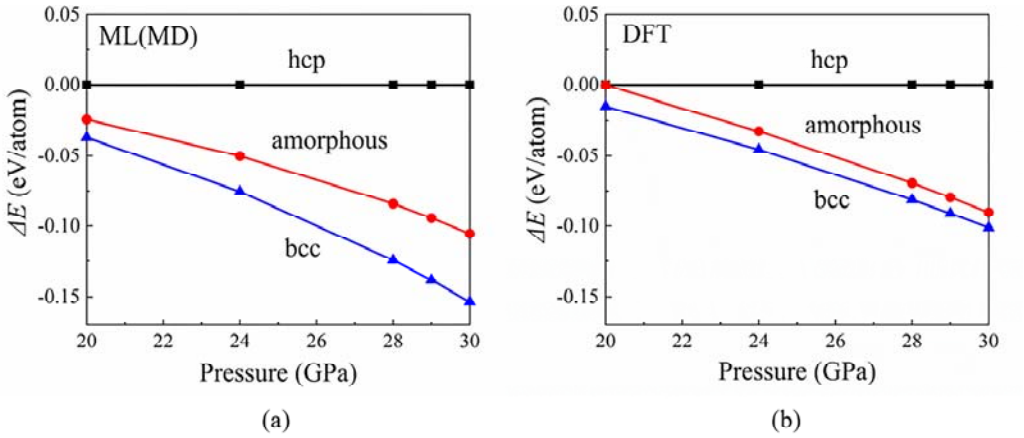

FIG. 13. Potential energies of hcp, bcc and amorphous solid as a function of *c*-axis uniaxial and hydrostatic pressure obtained from (a) machine learning interatomic potential and (b) DFT calculations. Our machine learning prediction is in line with the results of first principle calculations. Above 20 GPa, the uniaxial compressed amorphous metastable possesses a lower energy than that of [0001] uniaxial compressed hcp phase while a higher energy than the hydrostatic pressured bcc phase.